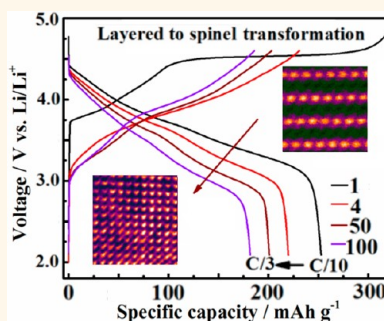# Formation of the Spinel Phase in the Layered Composite Cathode Used in Li-Ion Batteries

Meng Gu,[†] Ilias Belharouak,[‡] Jianming Zheng,[#] Huiming Wu,[‡] Jie Xiao,[#] Arda Genc,[§] Khalil Amine,[‡] Suntharampillai Thevuthasan,[†] Donald R. Baer,[†] Ji-Guang Zhang,[#] Nigel D. Browning,[⊥] Jun Liu,[⊥] and Chongmin Wang[†,*]

[†]Environmental Molecular Science Laboratory, [⊥]Fundamental and Computational Science Directorate, and [#]Energy and Environmental Directorate, Pacific Northwest National Laboratory, 902 Battelle Boulevard, Richland, Washington 99352, United States, [‡]Chemical Sciences and Engineering Division, Argonne National Laboratory, 9700 South Cass Avenue, Argonne, Illinois 60439, United States, and [§]FEI Company, 5350 NE Dawson Creek Drive, Hillsboro, Oregon 97124, United States

ABSTRACT Pristine Li-rich layered cathodes, such as $Li_{1.2}Ni_{0.2}Mn_{0.6}O_2$ and $Li_{1.2}Ni_{0.1}Mn_{0.525}Co_{0.175}O_2$, were identified to exist in two different structures: $LiMO_2$ $R\bar{3}m$ and Li_2MO_3 $C2/m$ phases. Upon 300 cycles of charge/discharge, both phases gradually transform to the spinel structure. The transition from $LiMO_2$ $R\bar{3}m$ to spinel is accomplished through the migration of transition metal ions to the Li site without breaking down the lattice, leading to the formation of mosaic structured spinel grains within the parent particle. In contrast, transition from Li_2MO_3 $C2/m$ to spinel involves removal of Li^+ and O^{2-}, which produces large lattice strain and leads to the breakdown of the parent lattice. The newly formed spinel grains show random orientation within the same particle. Cracks and pores were also noticed within some layered nanoparticles after cycling, which is believed to be the

consequence of the lattice breakdown and vacancy condensation upon removal of lithium ions. The AlF_3-coating can partially relieve the spinel formation in the layered structure during cycling, resulting in a slower capacity decay. However, the AlF_3-coating on the layered structure cannot ultimately stop the spinel formation. The observation of structure transition characteristics discussed in this paper provides direct explanation for the observed gradual capacity loss and poor rate performance of the layered composite. It also provides clues about how to improve the materials structure in order to improve electrochemical performance.

KEYWORDS: lithium ion battery · layered structure · spinel formation · phase transformation

Li-ion batteries have been widely used as an energy storage device for modern electric devices, grid application, and renewable energy.[1−7] Cathodes with a layered structure such as $Li_{1.2}Ni_{0.2}Mn_{0.6}O_2$ (LNMO) and $Li_{1.2}Ni_{0.1}Mn_{0.525}Co_{0.175}O_2$ (LNMCO) can provide much higher capacity than the traditional cathode materials such as $LiCoO_2$ and $LiMn_2O_4$ spinel.[8−12] Therefore, these layered structures are one of the most promising candidates for future heavy duty applications such as hybrid and electric vehicles. However, the application of these materials faces three fundamental challenges: (1) voltage instability, (2) capacity fading, and (3) slow charge/discharge rate. Collective experimental observations indicate these challenges are closely related to the structural characteristics of these materials, such as the crystal structure, spatial distribution

of cations, and phase stability upon lithium extraction and insertion. Structurally, these layered structures are often composed of the intergrowth of $LiMO_2$ $R\bar{3}m$ and Li_2MO_3 $C2/m$ phases.[7,13] Nevertheless, it is not clear how each individual phase affects the performance of these materials. Further, the cations are not necessarily uniformly distributed at nanometer scale. Recently, Gu et al.[7] reported a nanoscale phase separation caused by the preferential segregation of Ni atoms on the particle surface and boundaries in the layered lithium nickel manganese oxide cathode materials. They further predicted that the formation of the Ni-rich surface layer would affect the diffusion of Li ions, and thus possibly have an impact on the rate performance of this cathode.[7] Accompanying the extraction of Li from the Li_2MO_3 phase at the 4.5 V voltage plateau is

the release of oxygen and Li$^+$(removal of the Li$_2$O part).[2] However, the effect of the removal of the Li$_2$O part on the lattice stability has not been established. The layered-to-spinel transformation has long been postulated as an important factor to account for the capacity fading and poor rate performance of the layered structure materials.[2,9,10,13−17] However, it is not clear where the spinel phase nucleates and how the spinel phase grows on the consumption of the layered structured phase. The answers to these questions critically depends on the atomic level structural and chemical analysis of materials and their correlation with the cyclic performance of the battery. On the basis of atomic scale *Z*-contrast imaging, Xu *et al.* have found that the migration of transition metal (TM) cations into the Li layers can initiate the formation of spinel near the particle surface region.[15] Apparently, a far more detailed microscopic understanding of the phase transformation characteristics in these layered structures will lead to tailoring of the materials structure for better electrochemical performance.

In this paper, we use aberration-corrected scanning/ transmission electron microscopy (S/TEM) imaging and energy dispersive X-ray spectroscopy (EDS) to probe the atomic structure of the layer structured cathode materials before and after high voltage cycling.[18] The STEM high angle annular dark field (HAADF) detector collects all the incoherently scattered electrons. The image intensity of each atomic column reflects the average atomic number of each atomic column ($\sim Z^{1.5}$ to $Z^{1.8}$),[18] which is therefore termed as *Z*-contrast imaging and is chemical sensitive, allowing us to intuitively interpret the atomic structure changes directly. We found that both LNMO and LNMCO layer structured cathodes are a random mixing of LiMO$_2$ $R\bar{3}m$ and Li$_2$MO$_3$ $C2/m$ phases, with both phases able to coexist in a single nanoparticle. Extraction of Li from the lattice of the layer-structured material leads to lattice break down, crack and porosity formation, and nucleation and growth of spinel. Mechanistically, the formation of spinel from LiMO$_2$ $R\bar{3}m$ is distinctively different from the transition of Li$_2$MO$_3$ $C2/m$ to spinel.

RESULTS AND DISCUSSIONS

Electrochemical Performance Measurements. Cycling performance and the corresponding charge/discharge profile evolution of the lithium-rich cathode material LNMO and AlF$_3$-coated LNMCO are shown in Figure 1. During formation cycles at C/10, these electrode materials could deliver a capacity higher than 250 mAh g^{-1}. After three formation cycles, despite increasing the current density to C/3 and lowering the charge cutoff voltage to 4.6 V, a capacity of 220 mAh g^{-1} could still be achieved for LNMO. LNMO only shows gradual capacity decay in the first 100 cycles, with capacity retention
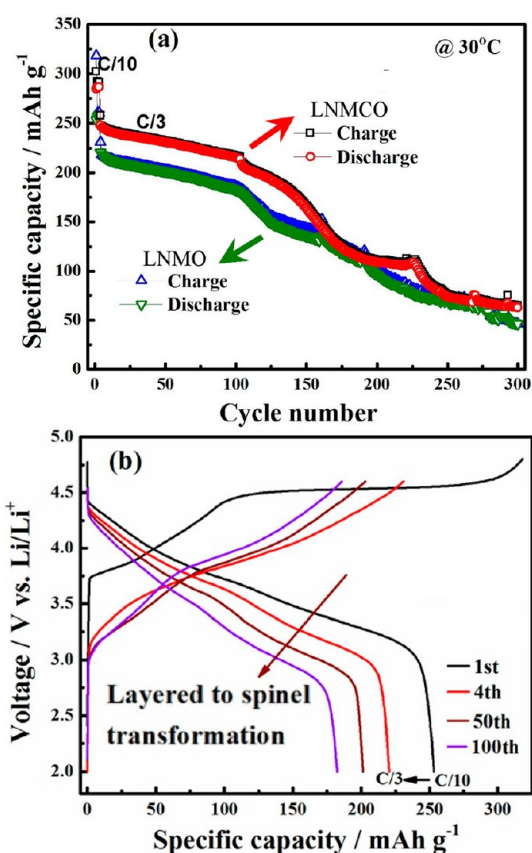

Figure 1. (a) Cycling performance of LNMO and AlF$_3$-coated LNMCO and (b) charge/discharge profiles of the LNMO cathode material.

of 82.8%. However, the material shows faster capacity fading after 100 cycles, which would be ascribed to the spinel transformation, lattice break down, and possible deteriorated electrode/electrolyte interface that hampers the reversible lithium ion intercalation/ deintercalation.[19−21] The AlF$_3$-coated-LNMCO exhibited higher capacity in most of the cycling range and the fast capacity decay is delayed to after $\sim$150 cycles. This means that the AlF$_3$ surface coating can partially relieve the formation of spinel phase in the layered structure, but it will not totally stop the spinel formation. The detailed voltage/capacity curves of an LNMO cathode at the first (C/10), and subsequent cycles at C/3 are presented in Figure 1b. The initial charge profile is accompanied with an irreversible voltage plateau at *ca*. 4.4−4.6 V for oxidation beyond the formal oxidation potential of Ni^{2+} to Ni^{4+}. The voltage plateaus have been assigned to an irreversible loss of oxygen from the lattice based on differential electrochemical mass spectrometry (DEMS) results[2,19] and *in situ* X-ray diffraction studies.[22] During the oxygen loss plateau, the Li$_2$MnO$_3$ component is activated and thus the material could deliver high discharge capacity during the subsequent discharge process. However, the extensive removal of the lithium ion and oxygen evolution results in the instability of the electrode structure,
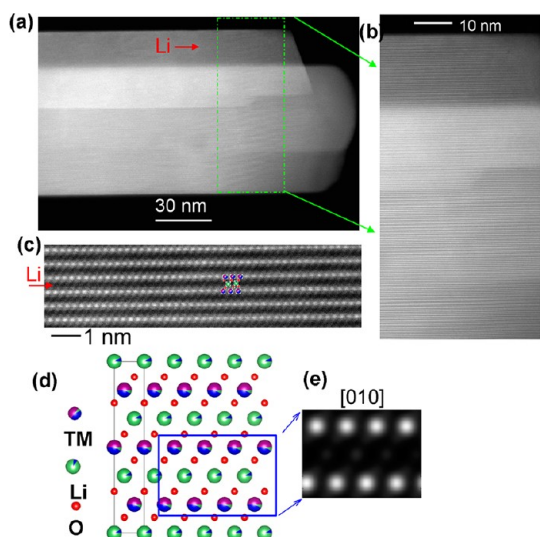
Figure 2. $R\bar{3}m$ phase (a) Overview Z-contrast image of the pristine LNMO cathode; (b) magnified image of the region shown as the green square in panel a; (c) atomic resolution image showing the Li-channels are very dark due to very small atomic number of Li, while TM cation has the highest intensity and oxygen ions are visible; (d) structural model of the [010] projection of the $R\bar{3}m$ phase; (e) simulated Z-contrast image the $R\bar{3}m$ phase based on a 10% Ni/Li disorder.

Figure 3. Li_2MO_3 $C2/m$ phase and atomic model of (a) Li_2MnO_3; (b) Ni-containing Li_2MO_3; (c) experimental Z-contrast image of the $C2/m$ phase; (d) [100], [110], [1−10] zone projection of the $C2/m$ phase; These zone axis projection regions are labeled with different colors lines in the image in panel c; these different zone axis regions in panel c are labeled with colored squares corresponding to the atomic model in panel d; the Li fast—diffusion channels are labeled with a red arrow in panel c.

involving lattice breakdown and phase transformation from layered to spinel during initial activation and subsequent cycling.[15,23] This structural transformation leads to a layered-spinel intergrowth structure and the evolution of the redox reaction at *ca.* 3.2 V region, as observed for $0.7Li_2MnO_3 \cdot 0.3LiNi_{1/3}Co_{1/3}Mn_{1/3}O_2$.[23] As a result, the discharge profile shows obvious voltage decay with the increase in cycle numbers. The midpoint voltage (MPV) of discharge decreases from 3.57 V at the fourth to 3.37 V at 100 cycles. Similar voltage/capacity curves are observed for LNMCO. The voltage profile decay, which signals the layered-to-spinel transformation, is further characterized by comparing pristine and cycled samples using S/TEM.

Structure of the Pristine Materials. The layered LNMO is a nanocomposite composed of the intergrowth of $LiMO_2$ $R\bar{3}m$ and Li_2MO_3 $C2/m$ phases (M denotes transiton metal cations) as shown in Figure 2 and Figure 3.[7,13] The pristine LNMO maintains a layered structure with the stacking sequence of TM/O/Li/O as illustrated in Figure 2a. There is ~10% (or less) Ni/Li disorder—Ni replaces 10% of the the Li ions in the Li layer and Li replaces 10% of the transition metal ions in the TM layer for the $R\bar{3}m$ phase.[24−26] Both Li and TM cations are in octahedral sites. As shown by the Z-contrast images in Figure 2, the pristine LNMO cathode shows nanoplate-like morphology with open Li fast-diffusion channels. The Li channel direction is labeled with a red arrow in Figure 2a. The magnified region in Figure 2b shows that the Li-diffusion channels are very dark in the Z-contrast image. The atomic
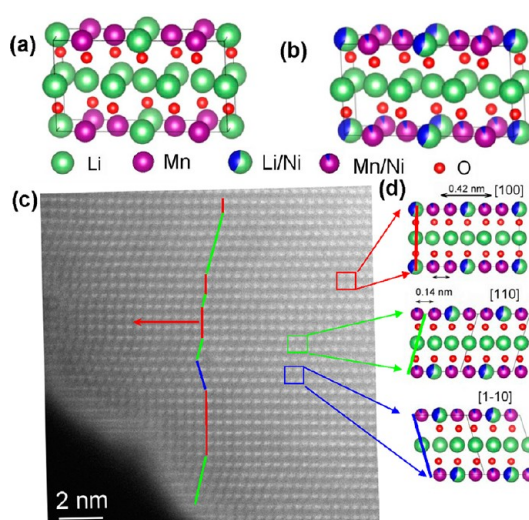
scale Z-contrast image in Figure 2c clearly shows that Li channels have the least intensity compared to the O sites or the brightest TM sites. The atomic resolution image in Figure 2c belongs to the [010] zone projection of the $R\bar{3}m$ phase (Figure 2d) with colored atoms labeled on each site. As proved by multislice image simulations shown in Figure 2e, the transition metal layer dominates the intensity in the Z-contrast image, while the Li layer is almost invisible.

The cation ordered Li_2MO_3 $C2/m$ phase has been observed to coexist with the $LiMO_2$ $R\bar{3}m$ phase even in a single nanoparticle. The atomic structural model of Li_2MO_3 $C2/m$ phase is shown in Figure 3. A comparison of Li_2MnO_3 phase and Ni-containing Li_2MO_3 phase is shown in Figure 3a,b. Ni occupies a portion of the Mn and Li sites in the TM layers. As representatively shown in the STEM-HAADF image of Figure 3, we noticed that some particles with the structure of Li_2MO_3 $C2/m$ possess different variants within the same particle. This is clearly demonstrated by the image shown in Figure 3d, where different domains are projected along a different zone axis within the same particle. The [100], [110], and [1−10] zone axis regions are labeled with red, green, and blue lines, respectively, in the experimental image, and the atomic model shown in Figure 3d. In addition, colored squares are used to match the atomic structure in the Z-contrast image to the atomic models shown in Figure 3d. The Li fast diffusion channels are labeled with a red arrow in Figure 3c. Clearly, the Li sites are too light to be detected in a Z-contrast image, thus, showing very dark intensity.
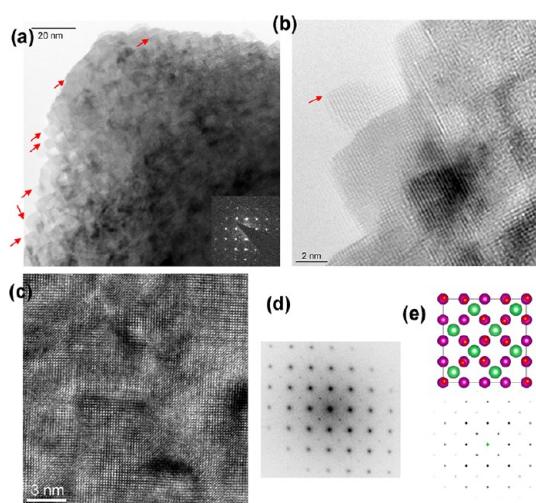
Figure 4. LNMO after 300 cycles (a) overview of the nanoparticle with spinel structure showing very well faceted steps in the surface; the inset shows the diffraction pattern (b) HRTEM image showing that a single crystal spinel projected along [001] zone axis. The spinel steps are well faceted in the {100} facets. The red arrows indicate the facets of the surface. (c) TEM image collected from the bulk region also revealed a cubic lattice after 60 cycles and (d) corresponding FFT at [001] zone; (e) atomic model and simulated diffraction pattern of the LiMn$_2$O$_4$ spinel [001] zone axis.

Formation of Spinel Phase from $R\overline{3}m$ Phase. The formation of LiMn$_2$O$_4$-type cubic spinel in the cycled sample has been identified by aberration corrected TEM along the [001] zone axis as shown in Figure 4a–e. After 300 charge/discharge cycles, the as-formed spinel exhibits faceted surface steps with {001} surfaces as indicated by the red arrows in Figure 4a. The inset of Figure 4d showed a TEM diffraction pattern, which exhibits cubic diffraction symmetry and matches the LiMn$_2$O$_4$-type spinel diffraction pattern in Figure 4e. The cubic spinel LiMn$_2$O$_4$ atomic model projected along the [001] zone is shown in Figure 4e with TM in a octahedral site and Li in the tetrahedral site. The HRTEM image in Figure 4b showed a lattice-resolution image of the surface steps with {001} facets. The TEM image collected from the bulk region in Figure 4c also revealed a cubic lattice, which corresponds to the cubic LiMn$_2$O$_4$-type spinel structure. The Fast Fourier transform (FFT) in Figure 4d of this HRTEM image matches the calculated diffraction pattern of LiMn$_2$O$_4$-type cubic spinel along the [001] zone axis in Figure 4e.

To trace the origin of the spinel formation, chemically sensitive Z-contrast imaging is utilized to analyze the atomic structure of the cycled samples. Migration of the TM cations into the Li layers has been detected after cycling as shown in Figure 5. The Li fast-diffusion path is labeled with a red arrow in Figure 5a–c. The higher magnification image from the surface region shown in Figure 5b reveals that the Li layer ions have an equivalent intensity compared to the transition metal layer. Toward the inner part of the particle, the Li layer
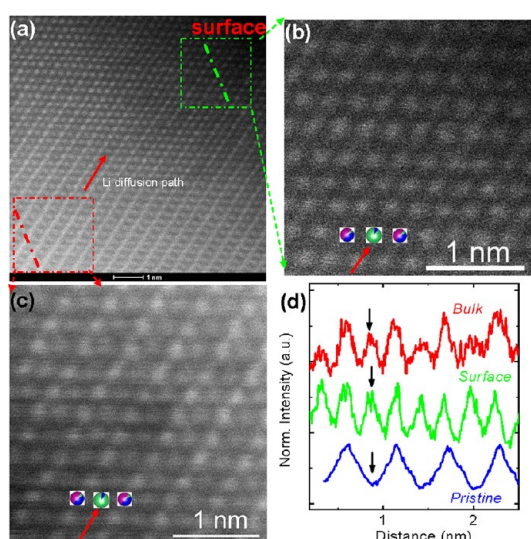

Figure 5. Cycled LNMO sample after 100 cycles: (a) overview Z contrast image of $R\overline{3}m$ phase region projected along [010] zone; higher magnification Z-contrast image showing the (b) surface region as labeled by the green square and (c) bulk region as labeled by the red square; (d) intensity line profile of the surface region as highlighted by the green line and bulk region as highlighted by the red line in image a, and pristine materials in Figure 2c. Note: the red arrows in the Z-contrast images show the Li fast diffusion path.

ions also show visible contrast. The Li layer in the pristine LNMO nanoparticle shows no visible contrast as illustrated in Figures 2c and 5d. However, following the charge/discharge cycles, the atomic columns in the Li layers both at the surface and in the bulk regions becomes visible, indicating the TM ions have migrated to the Li layer during the cyclic charge/discharge. As shown clearly in Figure 5d, the intensity of atomic columns in the Li layer at the surface region is stronger than that in the inner part of the particle in the cyclic charged/discharged sample. This observation likely indicates that the TM ions migration into the Li layer starts from the surface of the LNMO nanoparticles and extends to the inner region of the particle with the progression of the charge/discharge cycle. This conclusion is consistently supported by the observation reported by Xu et al.[15] They noticed that after high voltage cycling, the migration of the TM ions to the Li layers leads to the layered-to-spinel phase transformation, which only occurs at the very surface area of the particle. Essentially, they found that after 10 cycles, a few unit cells of spinel is formed at the surface region. For our present observation, the battery was charged/discharged to 100 cycles. Therefore the spinel formation extended to the inner part of the particle. Crystallographically, the transformation from layered $R\overline{3}m$ structure to spinel involves the migration of TM cations into the Li site, movement of Li cations into the tetrahedral sites, and a distortion of oxygen lattices.[9] The spinel phase formation facilitated by the migration of TM into the Li layer has an extremely low energy at low Li concentration during high voltage cycling.[15]
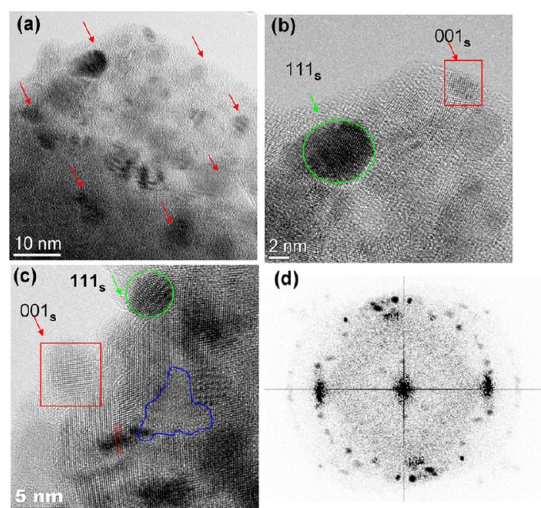
Figure 6. (a) Overview of the cathode after 60 cycles with small domains of spinel nucleated. (b and c) The nucleated spinel crystal domains have been found to be in different crystal orientation: [111] zone spinel is cycled in green, [001] zone spinel is labeled with a red square; area circled by blue is amorphous; the dashed lines indicate a dislocation. (d) FFT of the TEM image in panel c showing that the region is polycrystalline and the elongation of the diffraction spots indicates distortions of the lattices.

Associated with these structural transformation characteristics, the spinels formed within a parental layered particle show features of a mosaic structure as seen in Figure 4. Formation of spinel destroyed the layered characteristics of the $R\bar{3}m$ phase, which resulted in poor rate performance due to the block of the Li fast diffusion channel. This phase transformation is one of the primary factors contributing to the capacity fading and poor rate performance of these cathode materials.[15]

Ni concentration appears to play a role on the layered structure to spinel transformation.[27] Gu et al. used STEM and EDS mapping to analyze the composition and phase distribution in pristine LNMO.[7] The Li_2MO_3 phase contains Ni in most regions (~20% Ni/(Ni + Mn)) atomic ratio).[7] Hence, LNMO cannot be simply written as $0.5LiNi_{0.5}Mn_{0.5}O_2 \cdot 0.5Li_2MnO_3$. The average Ni/(Ni + Mn) ratio in the $LiMO_2$ phase should be less than 50% as in $LiNi_{0.5}Mn_{0.5}O_2$. The decreased Ni content may be one of the reasons that the $LiMO_2$ $R\bar{3}m$ phase transformed to spinel after cycling.[27] A very similar phase transformation process has also been identified in the LNMCO cathode after high voltage cycling.

Disoriented Spinel Domains Generation, Porosity and Crack Formation. In the cycled sample, spinel particles that are typically several nanometers show random orientation and are often found to be dispersed in an amorphous region as representatively shown in Figure 6. Most of the spinel domains are distributed with nanometer sizes within the whole particle (not only in the surface layer, but also in the bulk crystal) in Figure 6a.
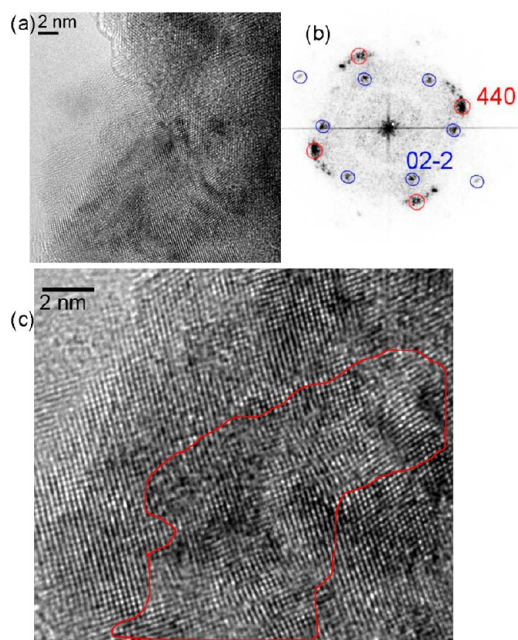

Figure 7. LNMO after 100 cycles (a) TEM images shows the distorted and polycrystalline lattices and (b) FFT of the image in panel a shows amorphous rings and diffractions spots corresponding to the $LiMn_2O_4$-type spinel in the [001] zone and [111] zone; the elongated circular spot region of 001 zone spots shows that there is a big amount of lattice distortions, which can also be observed in image c. The region highlighted in red in the TEM image (c) illustrates the lattice distortions.

These spinel domains are in different orientations with each other. For example, there are spinel domains in the [111] zone and [001] zone in Figure 6b,c. In between these domains are distorted lattice/amorphous phases as labeled by the blue area in Figure 6c, which may result from the strains associated with cation migration during cycling. Visualization of strain field within a solid material can be directly seen from the diffraction contrast of the TEM image. For the present case, the strain in the cycled sample can be seen by comparing the lattice image of pristine and cycled samples. The pristine layered cathode materials are characterized by perfect crystalline lattices without distortion as shown by Figures 2 and 3. However, the lattice of cycled samples exhibits a great amount of distortions—even amorphous in some regions as shown in Figures 4−7. Quantification of strain field in a single nanoparticle scale is not trivial. Therefore, no attempt was made to quantify the strain field. Formation of a dislocation labeled with dashed red lines is also observed in the distorted crystal matrix as shown in Figure 6c. The FFT of the image in Figure 6c exhibits a highly polycrystalline pattern, indicating the collapse of the layered cathode matrix. The lattice of the matrix breaks up into polycrystalline and amorphous regions. Figure 7 panels a and b show the HRTEM image and FFT pattern of a different region with spinel domain formation in [001] (diffraction spots

circled in red) and [111] (diffraction spots circled in blue) zone axis. The amorphous ring patterns indicate that amorphous regions must exist in this region in the TEM image in Figure 7a. A higher magnification TEM image is shown in Figure 7c, where the lattice shows a high degree of distortion in the phase boundaries of crystals with different orientations as labeled in red.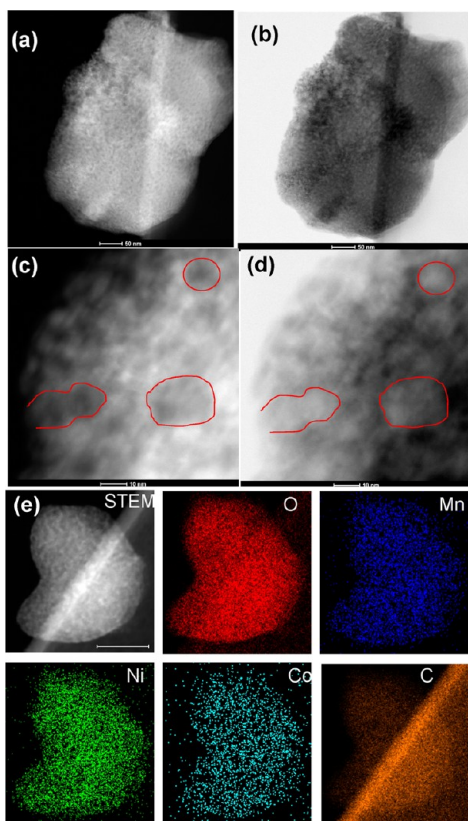 In the meantime, porosity formation has been detected in both the LNMO and LNMCO cathode nanoparticles. As shown in Figure 8, simultaneously taken Z-contrast and bright field images have been used to map the porosity formation in the cathode nanoparticles after cycling. Pores with sizes varying from 2 to 15 nm are distributed evenly in the LNMO nanoparticle (Figure 8a,b). In the Z-contrast image, the formation of pores would reduce the average atomic number of these regions, resulting in a darker contrast on the pore region. On the other hand, in the bright field image, the pore region shows up with brighter contrast according to the mass−thickness contrast theory. A detailed comparison of the contrast shown in the simultaneously acquired Z-contrast and bright field images is presented in Figure 8c,d. In addition, the formation of pores in the cycled LNMCO has also been seen and mapped out using EDS mapping in Figure 8e. The porosity formation may be related to the strain generation due to removal of Li or O upon cycling and collapse of the crystal lattices.[28] The surface of the LNCMO particles is covered with a uniformly thin layer of carbon-containing solid electrolyte layer as shown by the C map. In addition, the signatures of O, Mn, Ni, and Co are all observed by EDS mapping, confirming that this particle is truly the cathode nanoparticle.

Last but not least, crack formation has been found to exist as evidenced by the results of S/TEM imaging and EDS mapping in the cycled LNMCO samples in Figure 9. A comparison of the STEM Z-contrast image of the pristine LNMCO sample is shown in Figure S1 in the Supporting Information, which exhibits no such cracks. The cracks are labeled with red arrows in the STEM Z-contrast image in Figure 9. Crack formation has been reported by early researchers[28] and believed to originate from the large strain generated by removal of the cations during charging. As discussed above, the pristine cathode also contains the cation-ordered Li_2MO_3 phase. It has been reported that Li_2MO_3 can be activated and would release oxygen and lithium ions (in the form of Li_2O) during high voltage cycling.[2,14] We cannot exclude the possibility of crack formation

Figure 8. (a−d) Cycled LNMO and (e) LNMCO samples showing porosity formation after 60 cycles. (a) Z-contrast image; (b) bright field image; (c) higher magnification Z-contrast and (d) bright field image showing the contrast comparison of the pores in LNMO sample; (e) STEM Z-contrast image and EDS maps of cycled LNMCO sample. The scale bar in panel e is 30 nm and can be applied to all the elemental maps therein.
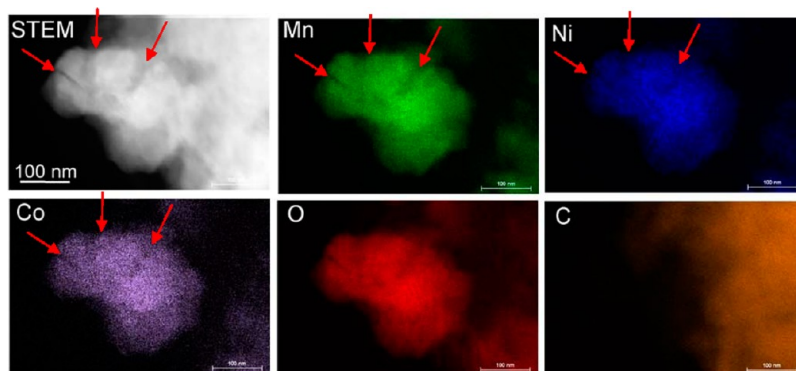

Figure 9. STEM and Mn, Ni, Co, O, C, EDS maps showing the crack formation in LNMCO after 60 cycles; the red arrows indicate the crack locations in the image and maps.
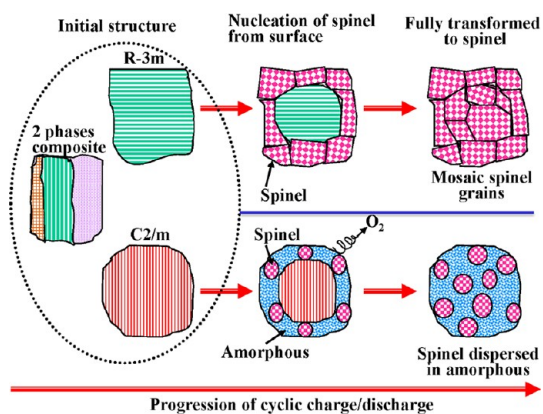
Figure 10. Schematic drawing showing that the initial material is composed of three phases: $R\bar{3}m$, $C2/m$, and nanocompsite of intergrowth of $R\bar{3}m$ and $C2/m$. The transition from the $R\bar{3}m$ and $C2/m$ layered structure to the spinel follows different routes, leading to different structural features of the spinel grains.

and lattice break-up in the $LiMO_2$ $R\bar{3}m$ phase region due to the Li^+ removal during high voltage cycling. The overall phase transformation characteristic of the layer structured materials is schematically shown in Figure 10. The layered-to-spinel transformation process is achieved either by cation migration in the stable $R\bar{3}m$ phase region, or the nucleation and growth mechanism in an polycrystalline/amorphous matrix in the $C2/m$ phase region after lattice break-up upon cyclic charge/discharge. The layered-to-spinel transformation, lattice break-up, and porosity formation are striking observations, which explain the loss of capacity during cycling in the Li-ion batteries. A lot of research effort has been made intending to stabilize the structure of the cathode materials during the cyclic charge/discharge. Coating of a surface layer on the particles of the cathode and modification of the chemistry of the cathode materials appear to prevent such a phase transformation in some way. However, the exact mechanism of the stabilization of the structure by the surface coating or the chemical additive is not clear. Typically, in the present work, a thin layer of AlF_3 coating on the surface of the LNMCO leads to a better capacity retention as illustrated in Figure 1. The surface layer coating may relieve the formation of spinel in the $R\bar{3}m$ phase. However, it cannot stop the formation of spinel in the $C2/m$, where the phase transformation proceeds through nucleation and growth process. More systematic work is needed to fully understand the mechanism of the surface coating on the lattice stability of cathode materials.

CONCLUSIONS

The LNMO and LNMCO layered cathode materials consist of an intergrowth of $LiMO_2$ $R\bar{3}m$ and Li_2MO_3 $C2/m$ phases. Migration of TM cations into the Li layer initiated the transformation to spinel for the $R\bar{3}m$ phase region during cycling. However, the Li_2MO_3 phase releases the Li_2O portion during high voltage cycling, resulting in the breakdown of the crystal lattices. As a result, lattice distortion/amorphization, crack formation, and porosity formation are clearly observed as evidenced by the S/TEM imaging and EDS mapping. In this case, the layered-to-spinel phase transformation follows a nucleation and growth mechanism, which yields spinel clusters with different orientations in the distorted/amorphized lattices. Coatings of the surface of cathode particles with AlF_3 may delay the formation of spinel in the $R\bar{3}m$ phase. Nevertheless, it cannot stop the formation of spinel in the $C2/m$ phase, where the phase transformation proceeds through nucleation and growth of spinel domains inside the broken lattice upon cycling. The structural changes of the layered structures observed in this work are believed to be the main factors influencing the capacity fading and poor rate performance of these layer-structured cathode materials.

METHODS

The LNMO and LNMCO were synthesized *via* a coprecipitation method.[29] Nickel sulfate hexahydrate ($NiSO_4.6H_2O$), manganese sulfate monohydrate ($MnSO_4.H_2O$), sodium hydroxide (NaOH), and ammonium hydroxide ($NH_3.H_2O$) were used as the starting materials to prepare $Ni_{0.25}Mn_{0.75}(OH)_2$ or $Ni_{0.125}Mn_{0.656}Co_{0.219}(OH)_2$ precursor. The precursors were well mixed with Li_2CO_3 and then calcined at 900 °C for 15 h to get the cathode materials. For electrochemical measurement, the cathode electrodes were prepared by coating a mixture containing 80% $Li[Li_{0.2}Ni_{0.2}Mn_{0.6}]O_2$, 10% super P (from Timcal), and 10% poly-(vinylidene fluoride) (PVDF, Kynar HSV900, Arkema Inc.) binder onto Al current collector foil. After drying, the electrodes were punched into disks with ø = 1.27 cm. The active material loading was 3−5 mg cm^{-2}. Coin cells were assembled with the cathode electrodes as-prepared, metallic lithium foil as counter electrode, Celgard K1640 monolayer polyethylene (PE) membrane as separator, and 1 M lithium hexafluorophosphate ($LiPF_6$)

dissolved in ethyl carbonate (EC) and dimethyl carbonate (DMC) (1:2 in volume) as electrolyte in an argon-filled MBraun glovebox. The electrochemical performance tests were performed galvanostatically between 2.0 and 4.6 V at $C/3$ ($1C = 250$ mA g^{-1}) after three formation cycles at $C/10$ between 2.0 and 4.8 V on an Arbin BT-2000 battery tester at a controlled temperature of 30 °C. Microstructures of the freshly prepared and electrochemically tested materials were analyzed using a probe-aberration corrected FEI Titan STEM and image-corrected FEI ETEM at 300 kV. The EDS maps were acquired using a 200 kV FEI Tecnai Osiris S/TEM microscope equipped with a FEI Super-X detector system, which combines four symmetrically placed Si drift detectors (SDD) around the objective lens with a high-brightness gun. This combination provides enhanced generation of X-rays and together with high detector efficiency results in a faster mapping of larger areas in EDS maps. In this work, the EDS maps with 512 × 512 pixels are obtained within less than 5 min. This helps to reduce specimen damage as the beam is not parked on any specimen region for a long period of time. The atomic

models are built using the VESTA software suite. The cycled samples are carried to the TEM within a sealed Ar atmosphere and the turbo-pump of the S/TEM microscope is prepumped to full speed so that the total air exposure time is less than 10 s.

Conflict of Interest: The authors declare no competing financial interest.

Supporting Information Available: The Supporting Information includes STEM image of the pristine LNMCO cathode nanoparticles. No cracks are visible in the pristine particles. This material is available free of charge *via* the Internet at http://pubs.acs.org.

REFERENCES AND NOTES

1. Armstrong, A. R.; Bruce, P. G. Synthesis of Layered LiMnO$_2$ as an Electrode for Rechargeable Lithium Batteries. *Nature* **1996**, *381*, 499–500.

2. Armstrong, A. R.; Holzapfel, M.; Novák, P.; Johnson, C. S.; Kang, S.-H.; Thackeray, M. M.; Bruce, P. G. Demonstrating Oxygen Loss and Associated Structural Reorganization in the Lithium Battery Cathode Li[Ni$_{0.2}$Li$_{0.2}$Mn$_{0.6}$]O$_2$. *J. Am. Chem. Soc.* **2006**, *128*, 8694–8698.

3. Armstrong, A. R.; Lyness, C.; Panchmatia, P. M.; Islam, M. S.; Bruce, P. G. The Lithium Intercalation Process in the Low-Voltage Lithium Battery Anode Li$_{1+x}$V$_{1-x}$O$_2$. *Nat. Mater.* **2011**, *10*, 223–229.

4. Ceder, G.; Chiang, Y. M.; Sadoway, D. R.; Aydinol, M. K.; Jang, Y. I.; Huang, B. Identification of Cathode Materials for Lithium Batteries Guided by First-Principles Calculations. *Nature* **1998**, *392*, 694–696.

5. Chiang, Y.-M. Building a Better Battery. *Science* **2010**, *330*, 1485–1486.

6. Gu, M.; Li, Y.; Li, X.; Hu, S.; Zhang, X.; Xu, W.; Thevuthasan, S.; Baer, D. R.; Zhang, J.-G.; Liu, J.; *et al.* *In situ* Tem Study of Lithiation Behavior of Silicon Nanoparticles Attached to and Embedded in a Carbon Matrix. *ACS Nano* **2012**, 8439–8447.

7. Gu, M.; Belharouak, I.; Genc, A.; Wang, D.; Wang, Z.; Amine, K.; Gao, F.; Zhou, G.; Thevuthasan, S.; Baer, D. R.; *et al.* Conflicting Roles of Ni in Controlling Cathode Performance in Li-Ion Batteries. *Nano Lett.* **2012**, 5186–5191.

8. Yu, C.; Guan, X.; Li, G.; Zheng, J.; Li, L.; Novel, A. Approach to Composite Electrode 0.3Li$_2$MnO$_3$−0.7LiMn$_{1/3}$Ni$_{1/3}$Co$_{1/3}$O$_2$ in Lithium-Ion Batteries with an Anomalous Capacity and Cycling Stability at 45.4°C. *Scr. Mater.* **2012**, *66*, 300–303.

9. Ito, A.; Shoda, K.; Sato, Y.; Hatano, M.; Horie, H.; Ohsawa, Y. Direct Observation of the Partial Formation of a Framework Structure for Li-Rich Layered Cathode Material Li[Ni$_{0.17}$Li$_{0.2}$Co$_{0.07}$Mn$_{0.56}$]O$_2$ Upon the First Charge and Discharge. *J. Power Sources* **2011**, *196*, 4785–4790.

10. Hong, J.; Seo, D.-H.; Kim, S.-W.; Gwon, H.; Oh, S.-T.; Kang, K. Structural Evolution of Layered Li$_{1.2}$Ni$_{0.2}$Mn$_{0.6}$O$_2$ Upon Electrochemical Cycling in a Li Rechargeable Battery. *J. Mater. Chem.* **2010**, *20*, 10179–10186.

11. Kim, J. H.; Sun, Y. K. Electrochemical Performance of Li[Li$_x$Ni$_{(1−3x)/2}$Mn$_{(1+x)/2}$]O$_2$ Cathode Materials Synthesized by a Sol−Gel Method. *J. Power Sources* **2003**, *119–121*, 166–170.

12. Fell, C. R.; Carroll, K. J.; Chi, M.; Meng, Y. S. Synthesis−Structure−Property Relations in Layered, Li-Excess Oxides Electrode Materials Li[Li$_{(1/3-2x/3)}$Ni$_x$Mn$_{(2/3-X/3)}$]O$_2$ (*X* = 1/3, 1/4, and 1/5). *J. Electrochem. Soc.* **2010**, *157*, A1202–A1211.

13. Lu, Z.; Beaulieu, L. Y.; Donaberger, R. A.; Thomas, C. L.; Dahn, J. R. Synthesis, Structure, and Electrochemical Behavior of Li[Ni$_x$Li$_{1/3-2x/3}$Mn$_{2/3-X/3}$]O$_2$. *J. Electrochem. Soc.* **2002**, *149*, A778–A791.

14. Seo, H.; Lee, E.; Yi, C.-W.; Kim, K. The Synthesis and Electrochemical Properties of Lithium Manganese Oxide (Li$_2$MnO$_3$). *J. Electrochem. Sci. Technol.* **2011**, *2*, 180–185.

15. Xu, B.; Fell, C. R.; Chi, M.; Meng, Y. S. Identifying Surface Structural Changes in Layered Li-Excess Nickel Manganese Oxides in High Voltage Lithium Ion Batteries: A Joint Experimental and Theoretical Study. *Energy Environ. Sci.* **2011**, *4*, 2223–2233.

16. Deng, Z. Q.; Manthiram, A. Influence of Cationic Substitutions on the Oxygen Loss and Reversible Capacity of Lithium-Rich Layered Oxide Cathodes. *J. Phys. Chem. C* **2011**, *115*, 7097–7103.

17. Yu, D. Y. W.; Yanagida, K. Structural Analysis of Li$_2$MnO$_3$ and Related Li−Mn−O Materials. *J. Electrochem. Soc.* **2011**, *158*, A1015–A1022.

18. Pennycook, S. J. Z-contrast Transmission Electron Microscopy—Direct Atomic Imaging of Materials. *Annu. Rev. Mater. Sci.* **1992**, *22*, 171–195.

19. Zheng, J. M.; Zhang, Z. R.; Wu, X. B.; Dong, Z. X.; Zhu, Z.; Yang, Y. The Effects of AlF$_3$ Coating on the Performance of Li[Li$_{0.2}$Mn$_{0.54}$Ni$_{0.13}$Co$_{0.13}$]O$_2$ Positive Electrode Material for Lithium-Ion Battery. *J. Electrochem. Soc.* **2008**, *155*, A775–A782.

20. Zheng, J. M.; Wu, X. B.; Yang, Y. A Comparison of Preparation Method on the Electrochemical Performance of Cathode Material Li[Li$_{0.2}$Mn$_{0.54}$Ni$_{0.13}$Co$_{0.13}$]O$_2$ for Lithium Ion Battery. *Electrochim. Acta* **2011**, *56*, 3071–3078.

21. Zheng, J.; Zhu, D.; Yang, Y.; Fung, Y. The Effects of *N*-Methyl-*N*-Butylpyrrolidinium Bis(Trifluoromethylsulfonyl)-Imide-Based Electrolyte on the Electrochemical Performance of High Capacity Cathode Material Li[Li$_{0.2}$Mn$_{0.54}$Ni$_{0.13}$Co$_{0.13}$]O$_2$. *Electrochim. Acta* **2012**, *59*, 14–22.

22. Lu, Z.; Dahn, J. R. Understanding the Anomalous Capacity of Li/Li[Ni$_X$Li$_{(1/3-x/3)}$Mn$_{(2/3-X/3)}$]O$_2$ Cells Using *in situ* X-ray Diffraction and Electrochemical Studies. *J. Electrochem. Soc.* **2002**, *149*, A815.

23. Johnson, C. S.; Li, N.; Lefief, C.; Vaughey, J. T.; Thackeray, M. M. Synthesis, Characterization and Electrochemistry of Lithium Battery Electrodes: *X*Li$_2$MnO$_3$·(1−*X*)LiMn$_{0.333}$Ni$_{0.333}$Co$_{0.333}$O$_2$ (0 ≤ *X* ≤ 0.7). *Chem. Mater.* **2008**, *20*, 6095–6106.

24. Jarvis, K. A.; Deng, Z.-Q.; Allard, L. F.; Manthiram, A.; Ferreira, P. J. Atomic Structure of a Lithium-Rich Layered Oxide Material for Lithium-Ion Batteries: Evidence of a Solid Solution. *Chem. Mater.* **2011**, *23*, 3614–3621.

25. Reed, J.; Ceder, G. Charge, Potential, and Phase Stability of Layered Li(Ni$_{0.5}$Mn$_{0.5}$)O$_2$. *Electrochem. Solid State Lett.* **2002**, *5*, A145–A148.

26. Xiao, J.; Chernova, N. A.; Whittingham, M. S. Layered Mixed Transition Metal Oxide Cathodes with Reduced Cobalt Content for Lithium Ion Batteries. *Chem. Mater.* **2008**, *20*, 7454–7464.

27. Sun, Y.-K.; Myung, S.-T.; Park, B.-C.; Prakash, J.; Belharouak, I.; Amine, K. High-Energy Cathode Material for Long-Life and Safe Lithium Batteries. *Nat. Mater.* **2009**, *8*, 320–324.

28. Lei, C. H.; Bareno, J.; Wen, J. G.; Petrov, I.; Kang, S. H.; Abraham, D. P. Local Structure and Composition Studies of Li$_{1.2}$Ni$_{0.2}$Mn$_{0.6}$O$_2$ by Analytical Electron Microscopy. *J. Power Sources* **2008**, *178*, 422–433.

29. Wang, D.; Belharouak, I.; Koenig, G. M.; Zhou, G.; Amine, K. Growth Mechanism of Ni$_{0.3}$Mn$_{0.7}$CO$_3$ Precursor for High Capacity Li-Ion Battery Cathodes. *J. Mater. Chem.* **2011**, *21*, 9290–9295.